




# Molecular mechanism of $\beta$ -arrestin-2 pre-activation by phosphatidylinositol 4,5-bisphosphate

Kiae Kim  & Ka Young Chung  

## Abstract

Phosphorylated residues of G protein-coupled receptors bind to the N-domain of arrestin, resulting in the release of its C-terminus. This induces further allosteric conformational changes, such as polar core disruption, alteration of interdomain loops, and domain rotation, which transform arrestins into the receptor-activated state. It is widely accepted that arrestin activation occurs by conformational changes propagated from the N- to the C-domain. However, recent studies have revealed that binding of phosphatidylinositol 4,5-bisphosphate (PIP<sub>2</sub>) to the C-domain transforms arrestins into a pre-active state. Here, we aimed to elucidate the mechanisms underlying PIP<sub>2</sub>-induced arrestin pre-activation. We compare the conformational changes of  $\beta$ -arrestin-2 upon binding of PIP<sub>2</sub> or phosphorylated C-tail peptide of vasopressin receptor type 2 using hydrogen/deuterium exchange mass spectrometry (HDX-MS). Introducing point mutations on the potential routes of the allosteric conformational changes and analyzing these mutant constructs with HDX-MS reveals that PIP<sub>2</sub>-binding at the C-domain affects the back loop, which destabilizes the gate loop and  $\beta$ XX to transform  $\beta$ -arrestin-2 into the pre-active state.

**Keywords** Arrestin; Phosphatidylinositol 4,5-bisphosphate; Structure; HDX-MS

**Subject Categories** Membranes & Trafficking; Signal Transduction; Structural Biology

<https://doi.org/10.1038/s44319-024-00239-x>

Received 12 December 2023; Revised 9 July 2024;

Accepted 9 August 2024

Published online: 6 September 2024

## Introduction

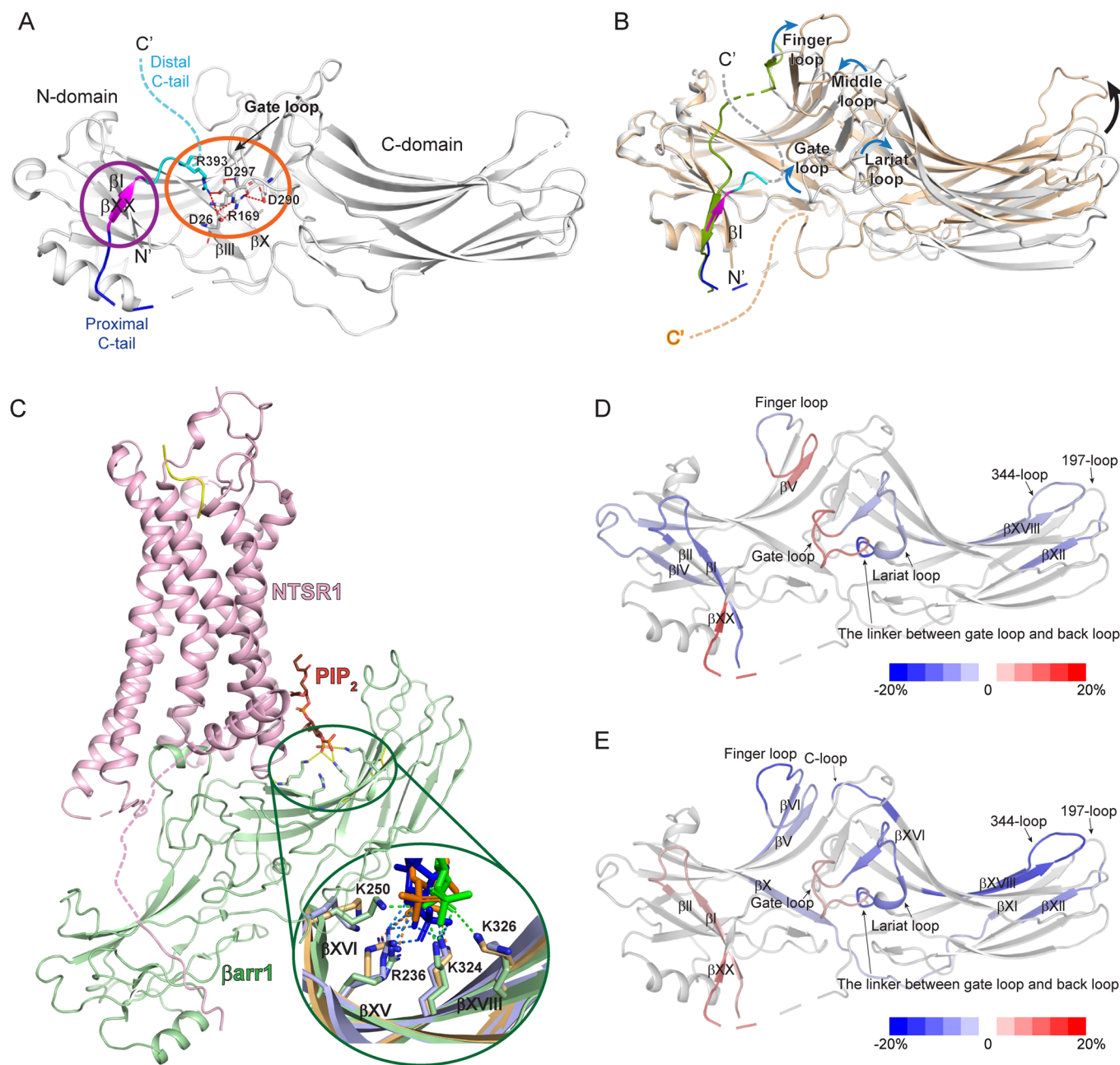
Arrestins, a protein family regulating G protein-coupled receptor (GPCR) signaling, have four distinct members in mammals (arrestin-1–4) (Benovic et al, 1987; Lohse et al, 1990). Arrestin-1 and -4 are visual system-specific, while arrestin-2 and -3 ( $\beta$ -arrestin-1 [ $\beta$ arr1] and 2 [ $\beta$ arr2]) are widely expressed (Lohse and Hoffmann, 2014). They desensitize and internalize agonist-activated phosphorylated GPCRs (Benovic et al, 1987) and regulate other signaling pathways (Coffa et al, 2011; Park et al, 2019; Perry-Hauser et al, 2022; Perry et al, 2019; Qu et al, 2021a; Smith and Rajagopal, 2016; Srivastava et al, 2015). Understanding how arrestins are activated at the structural and molecular level is crucial for the development of drugs targeting GPCRs or related pathways.

Previous studies revealed arrestin structures in basal and receptor-bound active states (Chen et al, 2023b; Hirsch et al, 1999; Huang et al, 2020b; Lee et al, 2020; Mayer et al, 2019; Park et al, 2019; Shukla et al, 2014; Staus et al, 2020; Yang et al, 2015; Yun et al, 2015; Zhou et al, 2017). Arrestins consist of N- and C-domains with a seven-stranded  $\beta$  sandwich in each domain (Fig. 1A). The basal state is stabilized by the interaction between the C-tail, more precisely  $\beta$ XX, and N-domain (Fig. 1A, purple circle) and the polar core formed by ionic interactions between residues within the gate loop,  $\beta$ III,  $\beta$ X, and C-tail (Fig. 1A, orange circle).

Binding of the phosphorylated GPCR (Fig. 1B, green) at the N-domain transforms arrestins into the active state by releasing  $\beta$ XX, disrupting the polar core, and affecting the conformation of the loops between the N- and C-domains, and altering the relative interdomain orientation (Fig. 1B). Although these conformational changes are the “canonical” changes of the receptor-activated arrestins, the degree of these changes can vary depending on the receptor types and phosphorylation patterns, resulting in different arrestin active states and functional outcomes (Kaya et al, 2020; Latorraca et al, 2020; Maharana et al, 2023b; Mayer et al, 2019; Yang et al, 2015; Zhou et al, 2017).

In recent years, plasma membrane components including phosphatidylinositol 4,5-bisphosphate (PIP<sub>2</sub>) have been implicated in  $\beta$ arr activation (Eichel et al, 2018; Grimes et al, 2023; Huang et al, 2020b; Janetzko et al, 2022; Kang et al, 2015; Zhai et al, 2023). High-resolution structures of GPCR- $\beta$ arr complexes show  $\beta$ arr’s C-domain contacting lipids or detergents (Chen et al, 2023b; Staus et al, 2020), which facilitates GPCR- $\beta$ arr complex formation (Lally et al, 2017; Zhou et al, 2017). The involvement of PIP<sub>2</sub> in  $\beta$ arr activation has been extensively suggested. With the assistance of PIP<sub>2</sub>,  $\beta$ arr can become “catalytically activated” (i.e., active without receptor binding) (Eichel et al, 2018). A subsequent study proposed that PIP<sub>2</sub>-binding is necessary for certain GPCR- $\beta$ arr interactions and that PIP<sub>2</sub> promotes  $\beta$ arr activation (Janetzko et al, 2022). Notably, the cryo-electron microscopy structures showed PIP<sub>2</sub>-binding at the C-domain of  $\beta$ arr1 in the neurotensin receptor 1 (NTSR1)- $\beta$ arr1 and glucagon receptor (GCGR)- $\beta$ arr1 complexes (Fig. 1C) (Chen et al, 2023b; Huang et al, 2020b). However, the precise structural mechanism by which PIP<sub>2</sub> promotes arrestin activation remains unclear.

Nevertheless, only few studies examined PIP<sub>2</sub>-induced  $\beta$ arr conformational changes by labeling specific residues with a fluorophore or <sup>19</sup>F (Janetzko et al, 2022; Zhai et al, 2023). Here, we investigated PIP<sub>2</sub>-induced arrestin activation mechanism using hydrogen-deuterium exchange mass spectrometry (HDX-MS). HDX-MS monitors the exchange between the amide hydrogen in the protein and deuterium in the solvent, providing information



about the protein conformational dynamics (Bai et al, 1993; Mayne, 2016). We compared the conformational dynamics of the PIP<sub>2</sub>-induced and the phosphorylated C-tail peptide of the vasopressin receptor type 2 (V2Rpp)-induced active states of  $\beta$ arr2 and explored activation mechanisms through mutational studies.

## Results and discussion

### Conformational changes of $\beta$ arr2 upon PIP<sub>2</sub>-binding

To investigate PIP<sub>2</sub>-induced conformational changes of  $\beta$ arr2, purified  $\beta$ arr2 was incubated with water-soluble PIP<sub>2</sub> (150  $\mu$ M) as

described in the Methods. Subsequently, deuterium exchange was initiated on ice for various durations (10, 100, 1000, and 10,000 s). The peptic peptides used for the HDX-MS analyses are shown in Fig. EV1, and the HDX-MS data analyzed in the present study are summarized in Dataset EV1. To compare the PIP<sub>2</sub>-induced structural changes with phosphorylated GPCR-induced changes, we also examined the effects of V2Rpp (500  $\mu$ M), a well-established model system for understanding  $\beta$ arr interactions with phosphorylated receptor C-tails (Fig. 1B) (Latorraca et al, 2020; Mayer et al, 2019; Shukla et al, 2013b; Yang et al, 2015).

V2Rpp induced higher HDX in the N-terminal half of the finger loop, gate loop, and proximal C-tail through  $\beta$ XX (Figs. 1D and EV2, peptides 62–69, 292–302, and 382–389), and lower HDX in a few

**Figure 1. Structures of  $\beta$ arr in various states and HDX-MS profile changes upon the binding of V2Rpp or PIP<sub>2</sub> to  $\beta$ arr2.**

(A) Structure of  $\beta$ arr1 in the basal state (PDB: 1G4R) (Data ref: Han et al, 2001a; Han et al, 2001b). The basal state  $\beta$ arr1 is colored gray with the C-terminus colored blue (proximal C-tail), magenta ( $\beta$ XX), and cyan (distal C-tail). Unresolved regions are indicated by dotted lines. The interaction between  $\beta$ XX and the residues in the N-domain is indicated in the purple circle, and the polar core is denoted in the orange circle. Residues that are involved in the polar core formation are shown as sticks. (B) Comparison of the structure of  $\beta$ arr1 in basal (PDB: 1G4R) (Data ref: Han et al, 2001a; Han et al, 2001b) and V2Rpp-bound (PDB: 4JQ1) (Data ref: Shukla et al, 2013a; Shukla et al, 2013b) states. V2Rpp-bound  $\beta$ arr1 is colored light orange and V2Rpp is colored green. The color codes for the basal state of  $\beta$ arr1 are same as those of (A). The conformational changes of the loop regions are shown with blue arrows, and the domain rotation is indicated with a black arrow. (C) Structure of the NTSR1- $\beta$ arr1 complex (PDB: 6UP7) (Data ref: Huang et al, 2020a; Huang et al, 2020b). NTSR1 is colored light pink, and  $\beta$ arr1 is colored light green. PIP<sub>2</sub> is indicated with orange sticks. The residues that interact with PIP<sub>2</sub> are shown as sticks. In the enlarged green circle, various modes of interaction between  $\beta$ arr1 and PIP<sub>2</sub> are shown; PIP<sub>2</sub> in the NTSR1- $\beta$ arr1 complex (PDB: 6UP7) (Data ref: Huang et al, 2020a; Huang et al, 2020b) is colored orange, the interacting residues in  $\beta$ arr1 are colored light orange, and the ionic interactions between PIP<sub>2</sub> and  $\beta$ arr1 are shown as green dotted lines; PIP<sub>2</sub> in the GCGR1- $\beta$ arr1 complexes (PDB: 8JRU and 8JRV) (Data ref: Chen et al, 2023a; Chen et al, 2023b) is colored blue or green, the interacting residues in  $\beta$ arr1 are colored light blue or light green, and the ionic interactions between PIP<sub>2</sub> and  $\beta$ arr1 are shown as blue or orange dotted lines respectively. (D) HDX-MS profile comparison between the apo and V2Rpp-bound  $\beta$ arr2. The HDX-level differences (i.e., HDX levels of apo  $\beta$ arr2-HDX levels of V2Rpp-bound  $\beta$ arr2) are color-coded on the basal state structure of  $\beta$ arr2 (PDB: 3P2D) (Data ref: Zhan et al, 2011a; Zhan et al, 2011b). Results were derived from three independent experiments. (E) HDX-MS profile comparison between the basal and PIP<sub>2</sub>-bound  $\beta$ arr2. The HDX-level differences (i.e., HDX levels of apo  $\beta$ arr2-HDX levels of PIP<sub>2</sub>-bound  $\beta$ arr2) are color-coded on the basal state structure of  $\beta$ arr2 (PDB: 3P2D) (Data ref: Zhan et al, 2011a; Zhan et al, 2011b). Results were derived from three independent experiments (biological). The color-coded HDX-level differences are based on the maximum differences at any D<sub>2</sub>O incubation time point. The detailed HDX-MS data are summarized in Dataset EV1 and Fig. EV2.

regions within the N-domain ( $\beta$ I,  $\beta$ IV through  $\beta$ V, and C-terminal half of the finger loop; peptides 1–19, 41–55, and 70–76), domain interfaces (the lariat loop and the linker between the gate loop and back loop; peptides 281–291 and 303–306), and a few regions within the C-domain (197-loop and  $\beta$ XVIII; peptides 195–201 and 324–338) (Figs. 1D and EV2).

These HDX-MS data well-reflected the known V2Rpp-induced conformational changes of  $\beta$ arr2. V2Rpp (Fig. 1B, green) interacts at the N-domain groove and near  $\beta$ I. Thus, lower HDX levels of the V2Rpp-bound  $\beta$ arr2 at the N-domain (specifically,  $\beta$ I and C-terminal half of the finger loop) probe the V2Rpp-binding in these regions. In addition, V2Rpp-induced higher HDX levels in the gate loop and proximal C-tail through  $\beta$ XX indicate conformational changes resulting from  $\beta$ XX release and polar core disruption. The HDX-level changes at the domain interfaces suggest conformational changes in the loop regions at the domain interfaces and/or domain rotation upon V2Rpp-binding, and the changes at the C-domain may reflect long-range allosteric conformational changes transmitted from the N-domain V2Rpp-binding site.

As HDX-MS analysis effectively probed the V2Rpp-induced activation of  $\beta$ arr2, we sought to analyze the PIP<sub>2</sub>-induced conformational changes of  $\beta$ arr2. Based on the NTSR1- $\beta$ arr1 and GCGR- $\beta$ arr1 complex structures, PIP<sub>2</sub> can interact with positively charged residues at  $\beta$ XV (R236 in the  $\beta$ arr1 sequence),  $\beta$ XVI (K250 in the  $\beta$ arr1 sequence), and  $\beta$ XVIII (K324 and K326 in the  $\beta$ arr1 sequence) (Fig. 1C, inlet). The HDX-MS analysis revealed that the HDX levels at  $\beta$ XVIII become lower upon co-incubation with PIP<sub>2</sub> (Figs. 1E and EV2, peptide 324–338), implying the binding of PIP<sub>2</sub> to  $\beta$ arr2. However, the HDX levels of the peptides covering  $\beta$ XV (Figs. 1E and EV2, peptide 219–239) and  $\beta$ XVI (Figs. 1E and EV2, peptide 251–258) were not affected. This may be due to three reasons. First, as HDX monitors the buffer exposure of the amide hydrogens at the peptide backbone, HDX levels could not be affected if the binding occurs through the charge-charge interaction mediated by the amino acid side chains without altering the peptide backbone conformation. Second, the PIP<sub>2</sub>-interacting residues may differ slightly between the receptor-bound (i.e., the NTSR1- $\beta$ arr1 and GCGR- $\beta$ arr1 complexes) and unbound states (i.e., current study). Even in the receptor-bound states, PIP<sub>2</sub> interacted differently between the NTSR1-bound and GCGR-bound states

(Fig. 1C, inlet). Third, the reported  $\beta$ arr structures with PIP<sub>2</sub> are  $\beta$ arr1 structures (Fig. 1C), but in this study, we analyzed the conformation of  $\beta$ arr2. Therefore, the differences may stem from variations between these subtypes. Nevertheless, the HDX-MS data indicate that PIP<sub>2</sub> interacts at the positively charged region within the C-domain of  $\beta$ arr2.

Interestingly, PIP<sub>2</sub> induced higher HDX levels at  $\beta$ I, gate loop, and proximal C-tail through  $\beta$ XX (Figs. 1E and EV2, peptides 1–19, 292–302, and 382–389), which is the canonical feature of the  $\beta$ arr activation (i.e.,  $\beta$ XX release and polar core disruption) (Fig. 1B) (Kim et al, 2015; Shukla et al, 2014; Yun et al, 2015). Of note, the HDX levels of the PIP<sub>2</sub>-bound state at the gate loop and proximal C-tail through  $\beta$ XX were still lower than the V2Rpp-bound state (Fig. EV2, peptides 292–302 and 382–389), which suggests that the PIP<sub>2</sub>-bound state is not as fully active as the V2Rpp-bound state. Thus, these results suggest that the binding of PIP<sub>2</sub> destabilizes the gate loop and the interaction of  $\beta$ XX at the N-domain, which may transform  $\beta$ arr2 more amenable to be activated (i.e., pre-active state).

PIP<sub>2</sub>-induced HDX-level changes were also evident at the finger loop,  $\beta$ VI,  $\beta$ X through  $\beta$ XI, 197-loop, C-loop, lariat loop, and the linker between the gate loop and back loop (Figs. 1E and EV2, peptides 62–69, 70–76, 75–81, 168–186, 195–201, 246–250, 281–291, and 303–306). Although most of these regions were also affected by V2Rpp-binding, the HDX-MS profiles at the finger loop and its extension (i.e.,  $\beta$ VI) (Figs. 1E and EV2, peptides 62–69, 70–76, and 75–81) and the lariat and gate loops (Figs. 1E and EV2, peptides 281–291 and 292–302) differed between the V2Rpp- and PIP<sub>2</sub>-bound states, suggesting that these regions adopt different conformations between V2Rpp- and PIP<sub>2</sub>-bound states. Furthermore,  $\beta$ X through  $\beta$ XI and the C-loop were affected by PIP<sub>2</sub>, but not by V2Rpp (Figs. 1E and EV2, peptides 168–186 and 246–250).

### Distal C-tail of $\beta$ arr2 is not involved in PIP<sub>2</sub>-induced pre-activation

The HDX-MS data suggest that the interaction of PIP<sub>2</sub> at the C-domain affects the conformational dynamics of  $\beta$ I, gate loop, and  $\beta$ XX (Fig. 1E) potentially through the allosteric transmission of the conformational changes from the C-domain to the gate loop and  $\beta$ XX. Thus, we sought to understand the routes for the allosteric

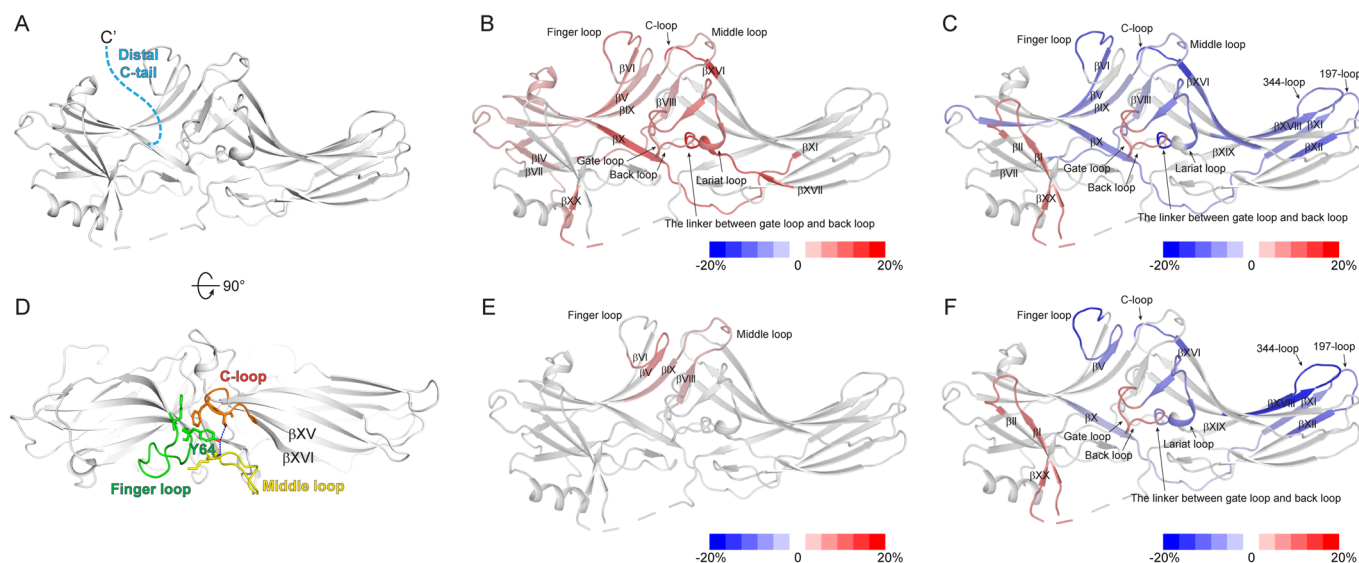


**Figure 2. HDX-MS profile analysis of  $\beta$ -arrestin-2 ( $\beta$ arr2)<sub>1-394</sub> and Y64.**

(A) The truncated distal C-tail of  $\beta$ arr2 is colored light blue on the basal state structure of  $\beta$ arr2 (PDB: 3P2D) (Data ref:Zhan et al, 2011a; Zhan et al, 2011b). (B) HDX-MS profile comparison between the WT and  $\beta$ arr2<sub>1-394</sub>. The HDX-level differences (i.e., HDX levels of WT  $\beta$ arr2-HDX levels of  $\beta$ arr2<sub>1-394</sub>) are color-coded on the basal state structure of  $\beta$ arr2 (PDB: 3P2D) (Data ref:Zhan et al, 2011a; Zhan et al, 2011b). Results were derived from three independent experiments (biological). (C) HDX-MS profile comparison between apo and PIP<sub>2</sub>-bound  $\beta$ arr2<sub>1-394</sub>. The HDX-level differences (i.e., HDX levels of apo  $\beta$ arr2<sub>1-394</sub> - HDX levels of PIP<sub>2</sub>-bound  $\beta$ arr2<sub>1-394</sub>) are color-coded on the basal state structure of  $\beta$ arr2 (PDB: 3P2D) (Data ref:Zhan et al, 2011a; Zhan et al, 2011b). Results were derived from three independent experiments (biological). (D) The top-view of the interaction between the finger, middle, and C-loops of  $\beta$ arr2 in the basal state (PDB: 3P2D) (Data ref:Zhan et al, 2011a; Zhan et al, 2011b). Y64 is indicated by green sticks. The finger, middle, and C-loops are green, yellow, and orange, respectively. (E) HDX-MS profiles of the WT and Y64A. HDX-level differences (i.e., HDX levels of WT  $\beta$ arr2-HDX levels of Y64A) are color-coded based on the basal state structure of  $\beta$ arr2 (PDB: 3P2D) (Data ref:Zhan et al, 2011a; Zhan et al, 2011b). Results were derived from three independent experiments (biological). (F) HDX-MS profile comparison of apo- and PIP<sub>2</sub>-bound Y64A. The HDX-level differences (i.e., HDX levels of apo Y64A-HDX levels of PIP<sub>2</sub>-bound Y64A) are color-coded based on the basal state structure of  $\beta$ arr2 (PDB: 3P2D) (Data ref:Zhan et al, 2011a; Zhan et al, 2011b). Results were derived from three independent experiments (biological). The color-coded HDX-level differences are based on the maximum differences at any D<sub>2</sub>O incubation time point. The detailed HDX-MS data are summarized in Dataset EV1 and Figs. EV3 and EV4.

conformational changes transmitted from the PIP<sub>2</sub>-binding sites to the gate loop or  $\beta$ XX.

The initial candidate was the distal C-tail (Fig. 2A). High-resolution structures have not fully characterized the distal C-tail because it is often unresolved or truncated (Han et al, 2001b; Hirsch et al, 1999; Zhan et al, 2011b). Nonetheless, given that the truncation of the distal C-tail transforms  $\beta$ arrs into the pre-active state (Celver et al, 2002; Gurevich, 1998; Gurevich et al, 1997; Kovoor et al, 1999), it is reasonable to hypothesize that the binding of PIP<sub>2</sub> perturbs the conformational dynamics of the distal C-tail to impact the activation status of  $\beta$ arrs. To test this hypothesis, we truncated the distal C-tail ( $\beta$ arr2<sub>1-394</sub>) and examined PIP<sub>2</sub>-induced HDX-level changes. If the distal C-tail serves as the route for allosteric conformational changes, PIP<sub>2</sub> should not affect HDX levels at the gate loop or  $\beta$ XX in  $\beta$ arr2<sub>1-394</sub>.

In the apo state, compared to the wild-type (WT),  $\beta$ arr2<sub>1-394</sub> exhibited higher HDX levels in numerous regions across the N- and C-domains (Figs. 2B and EV3), indicating that the distal C-tail truncation yields  $\beta$ arr2 conformationally more dynamic. This increased conformational dynamics, especially at the gate loop and  $\beta$ XX, accounts for the pre-active state, as previously reported (Celver et al, 2002; Gurevich, 1998; Gurevich et al, 1997; Kovoor et al, 1999).

PIP<sub>2</sub> induced HDX-level changes of  $\beta$ arr2<sub>1-394</sub> in the regions similar to the WT (compare Figs. 1E and 2C; Table EV1). Decreased HDX levels were detected at the PIP<sub>2</sub>-binding site

(Figs. 2C and EV3, peptide 324–338) and increased HDX levels were detected at  $\beta$ I, gate loop, and proximal C-tail through  $\beta$ XX (Fig. 2C and EV3, peptides 1–19, 292–302, and 382–389). These findings suggest that the PIP<sub>2</sub> can induce further activation of  $\beta$ arr2<sub>1-394</sub>.

Other regions altered in the WT were also similarly affected (Figs. 2C and EV3, peptides 70–76, 75–81, 168–186, 195–201, 246–250, 281–291, and 303–306). A few other regions where we did not observe HDX changes with PIP<sub>2</sub>-bound WT were also affected (Fig. EV3, peptides 50–64, 118–127, 128–145, and 251–258), but the HDX levels of these regions became statistically no different to those of the WT (Fig. EV3, peptides 128–145 and 251–258) or similar to those of the WT (Fig. EV3, peptides 50–64 and 118–127). In addition, we observed the decreased HDX levels at  $\beta$ XI (Figs. 2C and EV3, peptide 187–194). Overall, the HDX profile changes of the PIP<sub>2</sub>-bound  $\beta$ arr2<sub>1-394</sub> (Fig. 2C) were similar to those of the PIP<sub>2</sub>-bound WT (Fig. 1E), suggesting that the distal C-tail is not the route for allosteric conformational changes from the PIP<sub>2</sub>-binding sites to the gate loop or  $\beta$ XX.

### Y64 in the finger loop is not involved in PIP<sub>2</sub>-induced pre-activation

The finger, middle, and C-loops between the N- and C-domains undergo dramatic conformational changes upon activation (Fig. 1B) and interact with the cytosolic core of the receptor (Fig. 1C)

(Huang et al, 2020b; Kang et al, 2015). In the basal state, the finger, middle, and C-loops form a designated structure through hydrophobic and polar interactions (Fig. 2D). PIP<sub>2</sub> altered HDX levels in the finger loop and C-loop (Fig. 1E). Notably, the C-loop is located at the C-domain as an extension from the PIP<sub>2</sub>-binding sites ( $\beta$ XV and  $\beta$ XVI) (Figs. 1C and 2D). Therefore, our second hypothesis was that interactions between the finger, middle, and C-loops transmit the allosteric conformational changes. In the basal state, Y64 is located in a pocket formed by the finger-, middle-, and C-loops (Fig. 2D), probably stabilizing the interactions between these three loops. Thus, we reasoned that the mutation of Y64 destabilizes the interactions between these three loops and breaks off the transmission route from the PIP<sub>2</sub>-binding sites.

In the apo state, the mutation of Y64 to alanine (Y64A) altered HDX levels in the N-terminal half of the finger loop and middle loop compared to those in the WT (Figs. 2E and EV4, peptides 62–69 and 128–145), reflecting a disturbance of the conformation surrounding Y64, as expected. Upon addition of PIP<sub>2</sub>, Y64A displayed HDX changes in the regions similar to those of the WT (compare Figs. 1E and 2F; Table EV1). HDX levels were decreased at the PIP<sub>2</sub>-binding site (Figs. 2F and EV4, peptide 324–338) and increased at  $\beta$ I, gate loop, and proximal C-tail through  $\beta$ XX (Figs. 2F and EV4, peptides 1–19, 292–302, and 382–389). These findings suggest that PIP<sub>2</sub> can induce pre-activation of Y64A. Other

regions altered in the WT were also affected (Figs. 2F and EV4, peptides 62–69, 70–76, 168–186, 195–201, 246–250, 281–291, and 303–306). In addition, we observed decreased HDX levels at  $\beta$ XI (Fig. 2F and EV4, peptides 187–194). These results suggest that the interactions between the finger, middle, and C-loops are not routes for allosteric conformational transmission.

### The lariat loop of $\beta$ arr2 is involved in PIP<sub>2</sub>-induced pre-activation

Because the distal C-tail and the interactions between the finger, middle, and C-loops do not serve as routes for allosteric conformational transmission, we sought other potential routes. After careful examination of the basal state structure and HDX-MS data of PIP<sub>2</sub>-bound  $\beta$ arr2 (Figs. 1E and EV2), L280 in the lariat loop and E315 in the back loop were chosen as potential key residues (Fig. 3).

In the basal state, L280 faces the gate loop and forms hydrophobic interactions with L291, L295, and L302 (Fig. 3A), which stabilizes the conformation of the gate and lariat loops. If the allosteric conformational transmission is mediated through perturbation of the interaction of the lariat and gate loops, the L280 mutation would disrupt this route. To test this hypothesis, we mutated L280 to glycine.

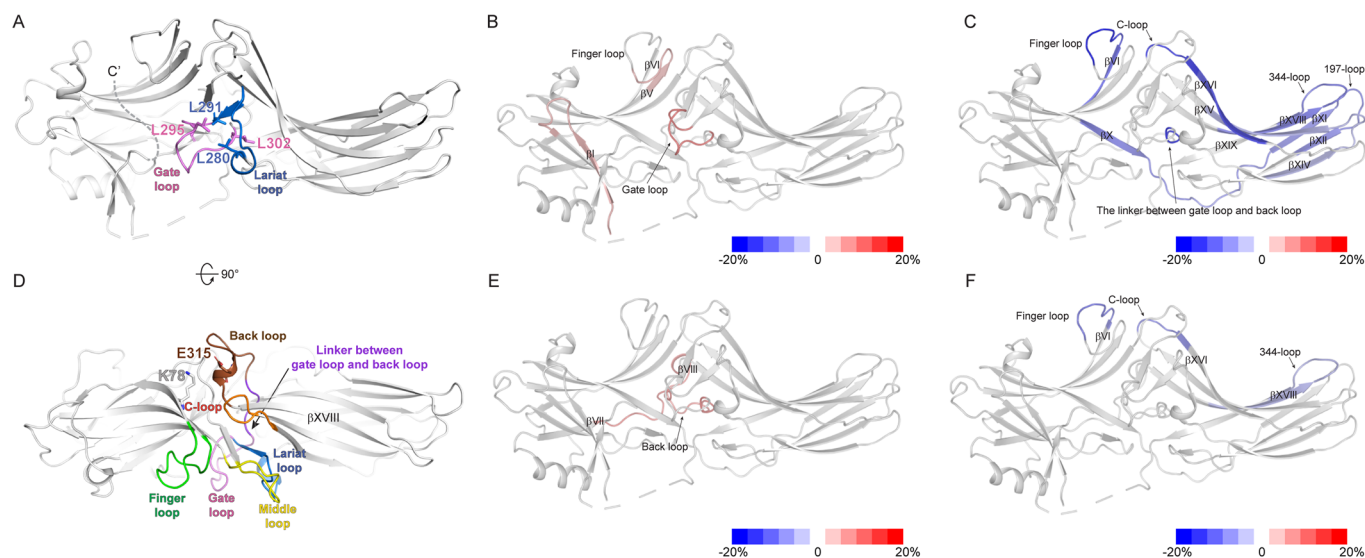


**Figure 3. HDX-MS profile analysis of L280 and E315.**

(A) Interaction between the lariat and gate loops in the basal state  $\beta$ arr2 (PDB: 3P2D) (Data ref:Zhan et al, 2011a; Zhan et al, 2011b). The lariat and gate loops are shown in blue and pink, respectively. The hydrophobic residues forming the interaction between the lariat and gate loops are shown as sticks. (B) HDX-MS profile comparison of the WT and L280G. The HDX-level differences (i.e., HDX levels of WT  $\beta$ arr2–HDX levels of L280G) are color-coded on the basal state structure of  $\beta$ arr2 (PDB: 3P2D) (Data ref:Zhan et al, 2011a; Zhan et al, 2011b). Results were derived from three independent experiments (biological). (C) HDX-MS profile comparison of apo and PIP<sub>2</sub>-bound L280G. The HDX-level differences (i.e., HDX levels of apo Y64A–HDX levels of PIP<sub>2</sub>-bound L280G) are color-coded on the basal state structure of  $\beta$ arr2 (PDB: 3P2D) (Data ref:Zhan et al, 2011a; Zhan et al, 2011b). Results were derived from three independent experiments (biological). (D) Top-view of the structure of the basal state  $\beta$ arr2 (PDB: 3P2D) (Data ref:Zhan et al, 2011a; Zhan et al, 2011b) showing relative positions of the back (brown), gate (pink), and lariat (blue) loops, and the linker between the gate and back loops (violet). E315 is shown as brown sticks, and K78 is shown as gray sticks. The finger, middle, and C-loops are colored green, yellow, and orange, respectively. (E) HDX-MS profile comparison between the WT and E315A. The HDX-level differences (i.e., HDX levels of WT  $\beta$ arr2–HDX levels of E315A) are color-coded on the basal state structure of  $\beta$ arr2 (PDB: 3P2D) (Data ref:Zhan et al, 2011a; Zhan et al, 2011b). Results were derived from three independent experiments (biological). (F) HDX-MS profile comparison of apo and PIP<sub>2</sub>-bound E315A. The HDX-level differences (i.e., HDX levels of apo Y64A–HDX levels of PIP<sub>2</sub>-bound E315A) are color-coded on the basal state structure of  $\beta$ arr2 (PDB: 3P2D) (Data ref:Zhan et al, 2011a; Zhan et al, 2011b). Results were derived from three independent experiments (biological). The color-coded HDX-level differences are based on the maximum differences at any D<sub>2</sub>O incubation time point. The detailed HDX-MS data are summarized in Dataset EV1 and Figs. EV4 and EV5.

In the apo state, L280G showed altered HDX levels at the gate loop (Figs. 3B and EV4, peptide 292–302), reflecting the altered conformation near the lariat and gate loop regions due to the mutation. L280G mutation also altered HDX levels at  $\beta$ I and the N-terminal half of the finger loop (Figs. 3B and EV4, peptides 1–19 and 62–69). The results suggest that perturbation of the interaction between the gate and the lariat loops could alter the conformational dynamics of remote regions, such as  $\beta$ I and finger loop.

Upon PIP<sub>2</sub>-binding to L280G, we observed decreased HDX levels at the PIP<sub>2</sub>-binding interface (Figs. 3C and EV4, peptide 324–338). We also observed altered HDX at the regions similar to those of the WT (compare Figs. 1E and 3C; Table EV1), such as the C-terminal half of the finger loop,  $\beta$ VI,  $\beta$ X through  $\beta$ XI, 197-loop, C-loop, and the linker between lariat loop and back loop (Figs. 3C and EV4, peptides 70–76, 75–81, 168–186, 195–201, 246–250, and 303–306). In addition, decreased HDX levels were evident at  $\beta$ XI,  $\beta$ XIV through  $\beta$ XV, and  $\beta$ XVI (Figs. 3C and EV4, peptides 187–194, 219–239, and 251–258).

In contrast, changes in HDX levels for  $\beta$ I, the gate loop, and proximal C-tail through  $\beta$ XX were not evident upon the binding of PIP<sub>2</sub> to L280G (Figs. 3C and EV4, peptides 1–19, 292–302, and 382–389). Therefore, the binding of PIP<sub>2</sub> in L280G induces conformational changes in most regions similar to those of the WT but failed to transform it to the pre-active conformation (i.e., disturbance of the gate loop and  $\beta$ XX), suggesting that perturbation of the interaction of the lariat and gate loops is the route for the transmission of the conformational changes from the PIP<sub>2</sub>-binding site to  $\beta$ XX.

### The back loop of $\beta$ arr2 is involved in PIP<sub>2</sub>-induced pre-activation

Another potential route we examined was the back loop. Although the HDX-MS profiles of the back loop were not affected by PIP<sub>2</sub>, the neighboring C-loop and the linker between the lariat and back loops were altered (Figs. 1E and EV2, peptides 246–250 and 303–306). Interestingly, the back loop is an extension of the PIP<sub>2</sub>-binding sites ( $\beta$ XVIII), located adjacent to the C-loop, and directly connected to the gate loop through the linker between the gate loop and the back loop (Fig. 3D). Previous evidence suggested that in the basal state, E315 at the back loop occasionally forms salt bridge with K78 at  $\beta$ VI (Fig. 3D) and that disruption of this interaction results in ligand-independent accumulation of  $\beta$ arr2 in the clathrin-coated endocytic structures (Eichel et al, 2018). Moreover, the back loop has been reported as a potential route for the conformational transition from PIP<sub>2</sub>-binding to  $\beta$ arr1 C-tail release (Zhai et al, 2023). Therefore, we further examined the role of the back loop in the PIP<sub>2</sub>-induced  $\beta$ arr2 activation.

To test this hypothesis, we mutated E315 to alanine, which would break the interaction between E315 and Y78 (Fig. 3D). In the apo state, compared to the WT, E315A showed higher HDX levels at the back loop and its neighboring  $\beta$ VII/ $\beta$ VIII loop (Figs. 3E and EV5, peptides 118–127 and 303–317) reflecting altered conformational dynamics of the back loop upon E315A mutation. As we did not observe HDX differences in other regions remote from the back loop, the results imply that the disruption of the interaction between E315 and K78 alters the local conformational dynamics but does not affect the overall conformational dynamics of  $\beta$ arr2.

Although the apo state did not show HDX-level differences between the WT and E315A other than in the back loop and  $\beta$ VII/

$\beta$ VIII loop, the effects of PIP<sub>2</sub> on E315A were dramatically different from those on the WT (compare Figs. 1E and 3F; Table EV1). Although PIP<sub>2</sub> induced a decrease in HDX levels at the PIP<sub>2</sub>-binding site in E315A (Figs. 3F and EV5, peptide 324–338), indicating PIP<sub>2</sub>-binding to E315A, we observed HDX-MS profile changes only within very limited regions, such as the C-terminal half of the finger loop and the C-loop (Figs. 3F and EV5, peptides 70–76 and 246–250) but no other regions. These results suggest that, in E315A, PIP<sub>2</sub> could alter the C-loop and its neighboring finger loop but fails to transform  $\beta$ arr2 to the pre-active state. Thus, we conclude that the PIP<sub>2</sub>-induced conformational changes are allosterically transmitted through the back loop to  $\beta$ XX.

### PIP<sub>2</sub> facilitates V2Rpp-induced $\beta$ arr2 activation

A recent study by Zhai et al reported that the simultaneous binding of V2Rpp and PIP<sub>2</sub> induces complex conformational changes in different structural regions (Zhai et al, 2023). Here, we tested whether pre-incubation with PIP<sub>2</sub> affects the V2Rpp-induced C-tail release. To examine the C-tail release of  $\beta$ arr2, we developed an experimental system using bimane fluorophore, an environment-sensitive fluorescent molecule. We substituted glycine at residue 6 to tryptophan (G6W) and labeled bimane at the  $\beta$ arr2 C-tail by substituting aspartate at residue 386 with cysteine (D386C) (Fig. 4A) in the cysteine-free  $\beta$ arr2 background (Cys-free  $\beta$ arr2: C17S/C60A/C126S/C141I/C151V/C244V/C253V/C271S/C405S/C410S). Bimane fluorescence can be quenched by nearby tryptophan residues (Jones Brunette and Farrens, 2014). Therefore, in the basal state, bimane fluorescence at the residue 386 is quenched by the tryptophan at the residue 6 (Fig. 4A, upper panel), but upon C-tail release, quenching is abolished as the residue 386 moves away from the residue 6 (Fig. 4A, lower panel).

When we incubated the bimane-labeled  $\beta$ arr2 with excess V2Rpp (300  $\mu$ M), bimane fluorescence increased (Fig. 4B), reflecting the C-tail release. To examine the pre-activation effect of PIP<sub>2</sub>, we reduced V2Rpp concentration to 30  $\mu$ M, where it induces minimal bimane fluorescence increase (Fig. 4C). Similarly, 30  $\mu$ M PIP<sub>2</sub> did not induce C-tail release (Fig. 4C). However, pre-incubation with PIP<sub>2</sub> followed by V2Rpp addition significantly increased the bimane fluorescence (Fig. 4C), implying that PIP<sub>2</sub> pre-incubation facilitates V2Rpp-induced  $\beta$ arr2 activation.

Introducing the L280G mutation to disrupt the allosteric conformational pathway reduced the augmentation of the V2Rpp-induced C-tail release after PIP<sub>2</sub> pre-incubation (Fig. 4C). This result confirms that the lariat loop is the allosteric conformational change route through which PIP<sub>2</sub> facilitates phosphorylated receptor-induced  $\beta$ arr2 activation.

### Proposed mechanism of the PIP<sub>2</sub>-induced $\beta$ arr2 activation

Here, we comprehensively analyzed the conformational dynamics of the whole  $\beta$ arr2 using HDX-MS. Our data confirmed that PIP<sub>2</sub>-bound  $\beta$ arr2 adopts the pre-active conformation, enhancing  $\beta$ arr2's interaction with V2Rpp. Interestingly, the PIP<sub>2</sub>-binding sites are remote from  $\beta$ XX and polar core (Fig. 4D), suggesting allosteric conformational transmission. The HDX-MS data suggested that both L280G and E315A failed to activate  $\beta$ arr2, but the

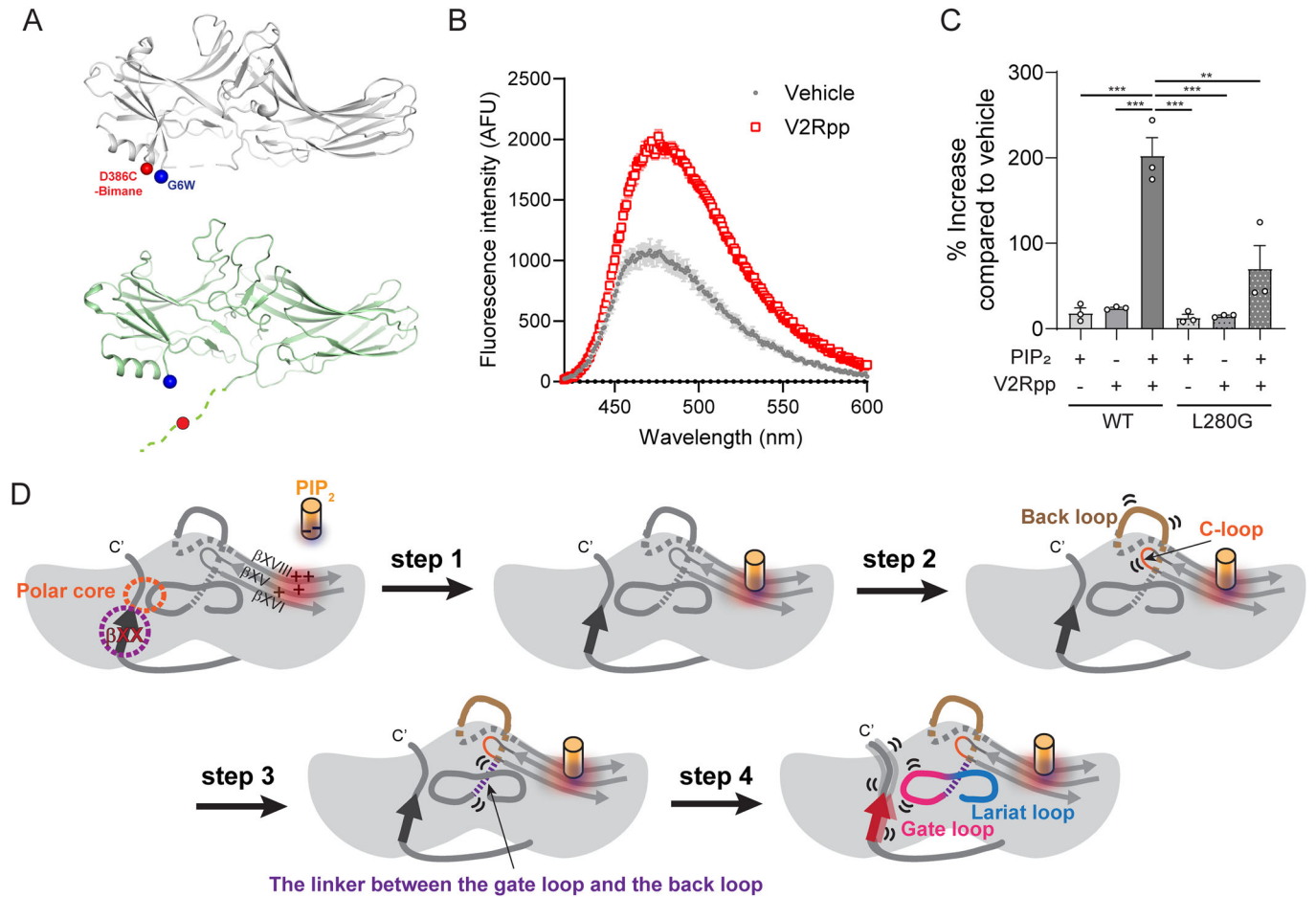


**Figure 4. Proposed molecular mechanism of  $\beta$ arr2 pre-activation upon PIP<sub>2</sub>-binding.**

(A) The scheme of the experimental system analyzing C-tail release. The position of residues 6 and 386 are shown as red and blue spheres in the basal state structure of  $\beta$ arr2 (upper panel, PDB: 3P2D) (Data ref: Zhan et al, 2011a; Zhan et al, 2011b) and V2Rpp-bound structure of  $\beta$ arr2 (lower panel, PDB: 8GOC) (Data ref: Maharana et al, 2023a; Maharana et al, 2023b). (B) Bimane fluorescence traces of basal and V2Rpp-bound states. (C) Bimane fluorescence changes of wild-type (WT) or L280G  $\beta$ arr2 upon addition of PIP<sub>2</sub>, V2Rpp, or PIP<sub>2</sub> pre-incubation followed by V2Rpp addition. The statistical significance of the differences was determined using one-way ANOVA followed by Tukey's posttest (\*\* $P < 0.001$  and \*\*\* $P < 0.0001$ ). Exact  $P$ -values between PIP<sub>2</sub>-WT vs. PIP<sub>2</sub>-V2Rpp-WT, V2Rpp-WT vs. PIP<sub>2</sub>-V2Rpp-WT, PIP<sub>2</sub>-V2Rpp-WT vs. PIP<sub>2</sub>-L280G, PIP<sub>2</sub>-V2Rpp-L280G, and PIP<sub>2</sub>-V2Rpp-WT vs. PIP<sub>2</sub>-V2Rpp-L280G are 0.000017, 0.000016, 0.000009, 0.000010, and 0.000317, respectively. Results were derived from three independent experiments (biological). Data are presented as mean  $\pm$  standard error of the mean. (D)  $\beta$ arr2 is shown schematically as a gray shape, particular regions are highlighted in dark gray (dotted) lines. Secondary structures (beta sheets) of interest are shown as arrows. The positively charged region in C-domain is indicated by red color and "+" symbols. PIP<sub>2</sub> is shown as the orange cylinder. In its basal state,  $\beta$ arr2 is stabilized through the interaction of  $\beta$ XX at the N-domain (dotted purple circle) and through the ionic interactions between N- and C-domains (i.e., polar core, dotted orange circle). The negatively charged PIP<sub>2</sub> binds to the positively charged region within the C-domain of  $\beta$ arr2 (step 1). This PIP<sub>2</sub>-binding induces alterations in the conformational dynamics of the back and C-loops (step 2). The resulting conformational change is transmitted to the linker between the gate loop and the back loop (step 3). Consequently, the conformational dynamics of the gate and lariat loops are altered, leading to the destabilization of the gate loop and  $\beta$ XX, ultimately resulting in the pre-activation of  $\beta$ arr2 (step 4).

two mutants exhibited different PIP<sub>2</sub>-induced conformational changes (Fig. 3). In L280G, PIP<sub>2</sub> could still induce conformational changes in almost all the regions similar to the WT, except the gate loop,  $\beta$ XX, and  $\beta$ I (Fig. 3C). In contrast, in E315A, the binding of PIP<sub>2</sub> induced conformational changes in only limited regions (i.e., the C-loop and its neighboring finger loop; Fig. 3F) without affecting other regions. Thus, we propose that the back loop precede the gate loop when the allosteric conformational changes are transmitted from the PIP<sub>2</sub>-binding site to  $\beta$ XX. In summary, the binding of PIP<sub>2</sub> at the C-domain (Fig. 4D, step 1) affects the loops (i.e., the back loop and C-loop) that are connected to the PIP<sub>2</sub>-binding  $\beta$ -strands (Fig. 4D, step 2). The altered

conformational dynamics of the back loop is allosterically transmitted to the lariat and gate loops to pre-activate  $\beta$ arr2 (Fig. 4D, step 4) through the linker between the gate and back loops (Fig. 4D, step 3).

### Limitations and future perspectives

This study highlights the structural mechanism of the PIP<sub>2</sub>-induced  $\beta$ arr2 pre-activation but has limitations. First, within the cell, arrestins interact with a variety of other components, including phospholipids, receptors, G proteins, and signaling proteins (Chen et al, 2023b; Grimes et al, 2023; Lally et al, 2017; Qu et al, 2021b;

Smith et al, 2021). Therefore, the PIP<sub>2</sub>- or V2Rpp-induced conformational changes of the purified  $\beta$ arr2 might be too simplistic compared to the complex nature within the cell. Second, our study couldn't detail the allosteric conformation changes at the atomic level. Advances in biophysical techniques, such as time-resolved Cryo-EM (Klebl et al, 2023), could provide deeper insights into the step-by-step conformational changes at the atomic level.

It has long been believed that the interaction of the phosphorylated GPCRs at the N-domain is the key process for arrestin activation (Edward Zhou et al, 2019; Gusach et al, 2023; Hilger et al, 2018; Maharana et al, 2022; Seyedabadi et al, 2021; Wisler et al, 2014; Zhao et al, 2017). However, now it is emerging that arrestin activation can be achieved through various processes. Inositol hexaphosphate (IP<sub>6</sub>) interacts at the phosphate sensor within the N-domain resulting  $\beta$ XX release to activate  $\beta$ arr2 and triggers further downstream signal transduction (Chen et al, 2017). PIP<sub>2</sub> has been suggested to interact at the C-domain to activate arrestins (Janetzko et al, 2022; Zhai et al, 2023), and here we further propose the structural mechanism of PIP<sub>2</sub>-induced arrestin pre-activation. As it is evident that arrestins can be activated via various routes, it is needed to investigate the structural differences and the functional consequences of the different active states of arrestins.

## Methods

### Reagents and tools table

Reagent/resource	Reference or source	Identifier or catalog number
<b>Experimental models</b>		
<i>E. coli</i> DH5 $\alpha$ Chemically Competent	Enzynomics	Cat# CP010
<i>E. coli</i> ROSETTA(DE3)	Novagen	Cat# 70954
<b>Recombinant DNA</b>		
pET28a-WT rat $\beta$ -arrestin-2	This study	N/A
pET28a- $\beta$ -arrestin_2_1-394	This study	N/A
pET28a- $\beta$ -arrestin_2_Y64A	This study	N/A
pET28a- $\beta$ -arrestin_2_L280G	This study	N/A
pET28a- $\beta$ -arrestin_2_E315A	This study	N/A
pET28b-rat $\beta$ -arrestin-2 _Cysfree_G6W_D386C	This study	N/A
pET28b-rat $\beta$ -arrestin-2 _Cysfree_G6W_L280G_D386C	This study	N/A
<b>Oligonucleotides and other sequence-based reagents</b>		
PCR primer: Y64A Forward: GTGCCTTCGCGCTGGCCGAGAAGACCTGGATG	Bionics	N/A
PCR primer: L280G Forward: CACCATAACCCCGCTGGGCAGTGACAACCGAGAGAAG	Bionics	N/A
PCR primer: E315A Forward: GAGGGAGCCAACAAGGCGGTGCTGGGAATCCTAG	Bionics	N/A
PCR primer: G6W Forward: CATATGGGTGAGAAGCCCTGGACCAGGGTCTTCAAG	Bionics	N/A
PCR primer: D386C Forward: CCAACTATGCCACAGACTGCATCGTGTGAGGAC	Bionics	N/A
<b>Chemicals, enzymes and other reagents</b>		
Protease inhibitor cocktail	BioVision	Cat# K272
Deuterium oxide	Cambridge isotope laboratories	Cat# DLM-11-100
Ni-IDA resin	Cytiva	Cat# 17057501

### $\beta$ arr2 expression and purification

All protein constructs for HDX-MS were cloned into the pET28a vector, and mutant rat  $\beta$ arr2 constructs for Trp-induced bimane fluorescence quenching experiments were cloned into the pET28b. The rat  $\beta$ arr2 constructs were transformed into *Escherichia coli* BL21 (DE3). Point mutations were prepared using site-directed mutagenesis. Expression and purification were performed as previously described (Park et al, 2019). Briefly, WT rat  $\beta$ arr2 and the mutants were grown in LB broth medium at 37 °C until the optical density at 600 nm reached 0.4–0.6. The bacteria were then induced with 30  $\mu$ M IPTG for 24 h at 16 °C. Proteins were purified using Ni-IDA resins and size-exclusion chromatography.

### Hydrogen/deuterium exchange

$\beta$ arr2 at a final concentration of 50  $\mu$ M in 20 mM HEPES pH 7.4, 150 mM NaCl, and 100  $\mu$ M Tris [2-carboxyethyl] phosphine hydrochloride was co-incubated with 500  $\mu$ M V2Rpp or 150  $\mu$ M PIP<sub>2</sub> for 1 h at room temperature. HDX was performed by mixing 2  $\mu$ L of protein (50  $\mu$ M) with 28  $\mu$ L of D<sub>2</sub>O buffer (20 mM HEPES pH 7.4, 150 mM NaCl, 100  $\mu$ M Tris [2-carboxyethyl] phosphine hydrochloride, and 10% glycerol in D<sub>2</sub>O) and incubating the mixture for 10, 100, 1000, and 10,000 s on ice. At the indicated time points, the reaction was quenched by adding 30  $\mu$ L of ice-cold quench buffer (60 mM NaH<sub>2</sub>PO<sub>4</sub> pH 2.01 and 10% glycerol) and snap-frozen on dry ice. Identical procedures were conducted for



Reagent/resource	Reference or source	Identifier or catalog number
Dimethyl sulfoxide	Duchefa	Cat# D1370
Leupeptin	Goldbio	Cat# L-010
Lysozyme	Goldbio	Cat# L-040
TCEP	Goldbio	Cat# TCEP
IPTG	Goldbio	Cat# I2481C
Kanamycin	Goldbio	Cat# K-120-10N
Chloramphenicol	Duchefa	Cat# C0113.0025
Pepsin column	Life Technologies	Cat# 2313100
DNase I	Roche	Cat# 11284932001
Benzamide	Sigma-Aldrich	Cat# 12072
Imidazole	Sigma-Aldrich	Cat# I2399
O8:O PI(4,5)P <sub>2</sub>	Avanti Polar Lipids	Cat# 850185
Zeba Desalt Spin Desalting Columns	Thermo Scientific	Cat# 89890
Bromobimane	MedChemExpress	Cat# HY-100041
V2Rpp	Tufts University Core Facility	N/A
<b>Software</b>		
Prism 8.0	Graphpad	graphpad.com
PyMol 2.3	Schrodinger	pymol.org
ProteinLynx Global Server 2.4	Waters	<a href="http://www.waters.com">www.waters.com</a>
DynamX 3.0	Waters	<a href="http://www.waters.com">www.waters.com</a>

nondeuterated samples using a H<sub>2</sub>O buffer comprising 20 mM HEPES, pH 7.4, 150 mM NaCl, and 10% glycerol in H<sub>2</sub>O.

## HDX-MS

HDX-MS and data analyses were conducted as previously described (Du et al, 2019; Qu et al, 2021a). Briefly, the quenched samples underwent online digestion by passage through an immobilized pepsin column (2.1 × 30 mm; Life Technologies, Carlsbad, CA, USA). The digested peptide fragments were collected on a C18 VanGuard trap column (1.7 mm × 30 mm; Waters, Milford, MA, USA), followed by ultra-pressure liquid chromatography using an ACQUITY UPLC C18 column (1.7 mm, 1.0 mm × 100 mm; Waters). All settings and conditions for the system, such as voltage, temperature, collision energy, and lockspray, were as previously reported (Du et al, 2019; Qu et al, 2021a). Peptic peptides from nondeuterated samples were identified using ProteinLynx Global Server 2.4 (Waters). To process HDX-MS data, the amount of deuterium in each peptide was determined by measuring the centroid of the isotopic distribution using DynamX 3.0 (Waters).

## Trp-induced bimane fluorescence quenching experiment

βarr2 was prepared at a final concentration of 8 μM or 20 μM in 20 mM HEPES pH 7.4, 150 mM NaCl, and co-incubated with a 10-fold molar excess of bromobimane for 1 h on ice. Excess dye was removed by buffer exchange using a desalting column. Then, βarr2 at a final concentration of 3 μM was co-incubated with V2Rpp for

1 h at room temperature, with or without pre-incubation of PIP<sub>2</sub>. The samples were placed in a MicroFluor 96-well fluorescent plate. The samples were excited at 390 nm, and the emitted fluorescence was measured from 420 to 600 nm using 1-nm step size by Synergy Neo or Synergy Neo2 (BioTek, Winooski, VT, USA).

## Statistical analysis

For HDX-MS analysis, mass differences >0.22 Da and 2% were considered significant. Student's *t* test was used to determine the statistically significant differences between individual time points. For Trp-induced bimane fluorescence quenching data, the significant differences were analyzed by one-way ANOVA followed by Tukey's posttest. The statistical analyses were performed by GraphPad Prism software (GraphPad, San Diego, CA, USA), and statistical significance was set at *P* < 0.05.

## Data availability

HDX-MS data have been deposited to ProteomeXchange Consortium via PRIDE43 partner repository with the set identifier PXD049391 (<https://www.ebi.ac.uk/pride/archive/projects/PXD049391>).

The source data of this paper are collected in the following database record: [biostudies:S-SCDT-10\\_1038-S44319-024-00239-x](https://biostudies.org/studies/S-SCDT-10_1038-S44319-024-00239-x).

Expanded view data, supplementary information, appendices are available for this paper at <https://doi.org/10.1038/s44319-024-00239-x>.

## Peer review information

A peer review file is available at <https://doi.org/10.1038/s44319-024-00239-x>

## References

- Bai Y, Milne JS, Mayne L, Englander SW (1993) Primary structure effects on peptide group hydrogen exchange. *Proteins: Struct Funct Bioinforma* 17:75–86
- Benovic JL, Kühn H, Weyand I, Codina J, Caron MG, Lefkowitz RJ (1987) Functional desensitization of the isolated beta-adrenergic receptor by the beta-adrenergic receptor kinase: potential role of an analog of the retinal protein arrestin (48-kDa protein). *Proc Natl Acad Sci USA* 84:8879–8882
- Celver J, Vishnivetskiy SA, Chavkin C, Gurevich VV (2002) Conservation of the phosphate-sensitive elements in the arrestin family of proteins. *J Biol Chem* 277:9043–9048
- Chen K, Zhang C, Lin S, Yan X, Cai H, Yi C, Ma L, Chu X, Liu Y, Zhu Y et al (2023a) Protein Data Bank. Structure of the glucagon receptor bound to beta-arrestin 1 in ligand-free state. <https://www.rcsb.org/structure/8JRU>
- Chen K, Zhang C, Lin S, Yan X, Cai H, Yi C, Ma L, Chu X, Liu Y, Zhu Y et al (2023b) Tail engagement of arrestin at the glucagon receptor. *Nature* 620:904–910
- Chen Q, Perry NA, Vishnivetskiy SA, Berndt S, Gilbert NC, Zhuo Y, Singh PK, Tholen J, Ohi MD, Gurevich EV et al (2017) Structural basis of arrestin-3 activation and signaling. *Nat Commun* 8:1427
- Coffa S, Breitman M, Hanson SM, Callaway K, Kook S, Dalby KN, Gurevich VV (2011) The effect of arrestin conformation on the recruitment of c-Raf1, MEK1, and ERK1/2 activation. *PLoS ONE* 6:e28723
- Du Y, Duc NM, Rasmussen SGF, Hilger D, Kubiak X, Wang L, Bohon J, Kim HR, Wegrecki M, Asuru A et al (2019) Assembly of a GPCR-G protein complex. *Cell* 177:1232–1242.e1211
- Edward Zhou X, Melcher K, Eric Xu H (2019) Structural biology of G protein-coupled receptor signaling complexes. *Protein Sci* 28:487–501
- Eichel K, Jullié D, Barsi-Rhyne B, Latorraca NR, Masureel M, Sibarita J-B, Dror RO, von Zastrow M (2018) Catalytic activation of  $\beta$ -arrestin by GPCRs. *Nature* 557:381–386
- Grimes J, Koszegi Z, Lanoiselee Y, Miljus T, O'Brien SL, Stepniwski TM, Medel-Lacruz B, Baidya M, Makarova M, Mistry R et al (2023) Plasma membrane preassociation drives beta-arrestin coupling to receptors and activation. *Cell* 186:2238–2255 e2220
- Gurevich VV (1998) The selectivity of visual arrestin for light-activated phosphorhodopsin is controlled by multiple nonredundant mechanisms. *J Biol Chem* 273:15501–15506
- Gurevich VV, Pals-Rylaarsdam R, Benovic JL, Hosey MM, Onorato JJ (1997) Agonist-receptor-arrestin, an alternative ternary complex with high agonist affinity. *J Biol Chem* 272:28849–28852
- Gusach A, García-Nafria J, Tate CG (2023) New insights into GPCR coupling and dimerisation from cryo-EM structures. *Curr Opin Struct Biol* 80:102574
- Han M, Gurevich VV, Vishnivetskiy SA, Sigler PB, Schubert C (2001a) Protein Data Bank. Structure of bovine beta-arrestin 1 (<https://www.rcsb.org/structure/1G4R>) [DATASET]
- Han M, Gurevich VV, Vishnivetskiy SA, Sigler PB, Schubert C (2001b) Crystal structure of  $\beta$ -arrestin at 1.9 Å: possible mechanism of receptor binding and membrane translocation. *Structure* 9:869–880
- Hilger D, Masureel M, Kobilka BK (2018) Structure and dynamics of GPCR signaling complexes. *Nat Struct Mol Biol* 25:4–12
- Hirsch JA, Schubert C, Gurevich VV, Sigler PB (1999) The 2.8 Å crystal structure of visual arrestin: a model for arrestin's regulation. *Cell* 97:257–269
- Huang W, Masureel M, Qu Q, Janetzko J, Inoue A, Kato HE, Robertson MJ, Nguyen KC, Glenn JS, Skiniotis G et al (2020a) Protein Data Bank. Structure of neurotensin receptor and beta-arrestin 1 complex. (<https://www.rcsb.org/structure/6UP7>) [DATASET]
- Huang W, Masureel M, Qu Q, Janetzko J, Inoue A, Kato HE, Robertson MJ, Nguyen KC, Glenn JS, Skiniotis G et al (2020b) Structure of the neurotensin receptor 1 in complex with  $\beta$ -arrestin 1. *Nature* 579:303–308
- Janetzko J, Kise R, Barsi-Rhyne B, Siepe DH, Heydenreich FM, Kawakami K, Masureel M, Maeda S, Garcia KC, von Zastrow M et al (2022) Membrane phosphoinositides regulate GPCR- $\beta$ -arrestin complex assembly and dynamics. *Cell* 185:4560–4573.e4519
- Jones Brunette AM, Farrens DL (2014) Distance mapping in proteins using fluorescence spectroscopy: tyrosine, like tryptophan, quenches bimane fluorescence in a distance-dependent manner. *Biochemistry* 53:6290–6301
- Kang Y, Zhou XE, Gao X, He Y, Liu W, Ishchenko A, Barty A, White TA, Yefanov O, Han GW et al (2015) Crystal structure of rhodopsin bound to arrestin by femtosecond X-ray laser. *Nature* 523:561–567
- Kaya AI, Perry NA, Gurevich VV, Iverson TM (2020) Phosphorylation barcode-dependent signal bias of the dopamine D1 receptor. *Proc Natl Acad Sci USA* 117:14139–14149
- Kim DK, Yun Y, Kim HR, Seo M-D, Chung KY (2015) Different conformational dynamics of various active states of  $\beta$ -arrestin1 analyzed by hydrogen/deuterium exchange mass spectrometry. *J Struct Biol* 190:250–259
- Klebl DP, Aspinnall L, Muench SP (2023) Time resolved applications for Cryo-EM; approaches, challenges and future directions. *Curr Opin Struct Biol* 83:102696
- Kovoor A, Celver J, Abdryashitov RI, Chavkin C, Gurevich VV (1999) Targeted construction of phosphorylation-independent  $\beta$ -arrestin mutants with constitutive activity in cells. *J Biol Chem* 274:6831–6834
- Lally CC, Bauer B, Selent J, Sommer ME (2017) C-edge loops of arrestin function as a membrane anchor. *Nat Commun* 8:14258
- Latorraca NR, Masureel M, Hollingsworth SA, Heydenreich FM, Suomivuori C-M, Brinton C, Townshend RJL, Bouvier M, Kobilka BK, Dror RO (2020) How GPCR phosphorylation patterns orchestrate arrestin-mediated signaling. *Cell* 183:1813–1825.e1818
- Lee Y, Warne T, Nehmé R, Pandey S, Dwivedi-Agnihotri H, Chaturvedi M, Edwards PC, García-Nafria J, Leslie AGW, Shukla AK et al (2020) Molecular basis of  $\beta$ -arrestin coupling to formoterol-bound  $\beta$ 1-adrenoceptor. *Nature* 583:862–866
- Lohse MJ, Benovic JL, Codina J, Caron MG, Lefkowitz RJ (1990)  $\beta$ -Arrestin: a protein that regulates  $\beta$ -adrenergic receptor function. *Science* 248:1547–1550
- Lohse MJ, Hoffmann C (2014) Arrestin interactions with G protein-coupled receptors. In: Gurevich VV (ed) *Arrestins—pharmacology and therapeutic potential*. Springer Berlin Heidelberg, Berlin, Heidelberg, pp 15–56
- Maharana J, Banerjee R, Yadav MK, Sarma P, Shukla AK (2022) Emerging structural insights into GPCR- $\beta$ -arrestin interaction and functional outcomes. *Curr Opin Struct Biol* 75:102406
- Maharana J, Sarma P, Yadav MK, Saha S, Singh V, Saha S, Chami M, Banerjee R, Shukla AK (2023a) Protein Data Bank. Structure of beta-arrestin2 in complex with a phosphopeptide corresponding to the human Vasopressin V2 receptor, V2R. (<https://www.rcsb.org/structure/8GOC>) [DATASET]
- Maharana J, Sarma P, Yadav MK, Saha S, Singh V, Saha S, Chami M, Banerjee R, Shukla AK (2023b) Structural snapshots uncover a key phosphorylation motif in GPCRs driving  $\beta$ -arrestin activation. *Mol Cell* 83:2091–2107.e2097
- Mayer D, Damberger FF, Samarasingharedy M, Feldmueller M, Vuckovic Z, Flock T, Bauer B, Mutt E, Zosel F, Allain FHT et al (2019) Distinct G protein-coupled receptor phosphorylation motifs modulate arrestin affinity and activation and global conformation. *Nat Commun* 10:1261
- Mayne L (2016) Chapter thirteen—hydrogen exchange mass spectrometry. In: Kelman Z (ed) *Methods in enzymology*. Academic Press, pp 335–356

- Park JY, Qu C-X, Li R-R, Yang F, Yu X, Tian Z-M, Shen Y-M, Cai B-Y, Yun Y, Sun J-P et al (2019) Structural mechanism of the arrestin-3/JNK3 interaction. *Structure* 27:1162–1170.e1163
- Perry NA, Kaoud TS, Ortega OO, Kaya AI, Marcus DJ, Pleinis JM, Berndt S, Chen Q, Zhan X, Dalby KN et al (2019) Arrestin-3 scaffolding of the JNK3 cascade suggests a mechanism for signal amplification. *Proc Natl Acad Sci USA* 116:810–815
- Perry-Hauser NA, Hopkins JB, Zhuo Y, Zheng C, Perez I, Schultz KM, Vishnivetskiy SA, Kaya AI, Sharma P, Dalby KN et al (2022) The two non-visual arrestins engage ERK2 differently. *J Mol Biol* 434:167465
- Qu C, Park JY, Yun MW, He Q-T, Yang F, Kim K, Ham D, Li R-R, Iverson TM, Gurevich VV et al (2021a) Scaffolding mechanism of arrestin-2 in the cRaf/MEK1/ERK signaling cascade. *Proc Natl Acad Sci USA* 118:e2026491118
- Qu C, Park JY, Yun MW, He QT, Yang F, Kim K, Ham D, Li RR, Iverson TM, Gurevich VV et al (2021b) Scaffolding mechanism of arrestin-2 in the cRaf/MEK1/ERK signaling cascade. *Proc Natl Acad Sci USA* 118:e2026491118
- Seyedabadi M, Gharghabi M, Gurevich EV, Gurevich VV (2021) Receptor-arrestin interactions: the GPCR perspective. *Biomolecules* 11:218
- Shukla AK, Manglik A, Kruse AC, Xiao K, Reis RI, Tseng W-C, Staus DP, Hilger D, Uysal S, Huang L-Y et al (2013a) Protein Data Bank. Structure of active beta-arrestin1 bound to V2Rpp (<https://www.rcsb.org/structure/4JQI>) [DATASET]
- Shukla AK, Manglik A, Kruse AC, Xiao K, Reis RI, Tseng W-C, Staus DP, Hilger D, Uysal S, Huang L-Y et al (2013b) Structure of active  $\beta$ -arrestin-1 bound to a G-protein-coupled receptor phosphopeptide. *Nature* 497:137–141
- Shukla AK, Westfield GH, Xiao K, Reis RI, Huang L-Y, Tripathi-Shukla P, Qian J, Li S, Blanc A, Oleskie AN et al (2014) Visualization of arrestin recruitment by a G-protein-coupled receptor. *Nature* 512:218–222
- Smith JS, Pack TF, Inoue A, Lee C, Zheng K, Choi I, Eiger DS, Warman A, Xiong X, Ma Z et al (2021) Noncanonical scaffolding of G( $\alpha$ h) and beta-arrestin by G protein-coupled receptors. *Science* 371:eaay1833
- Smith JS, Rajagopal S (2016) The  $\beta$ -arrestins: multifunctional regulators of G protein-coupled receptors. *J Biol Chem* 291:8969–8977
- Srivastava A, Gupta B, Gupta C, Shukla AK (2015) Emerging functional divergence of  $\beta$ -arrestin isoforms in GPCR function. *Trends Endocrinol Metab* 26:628–642
- Staus DP, Hu H, Robertson MJ, Kleinhenz ALW, Wingler LM, Capel WD, Latorraca NR, Lefkowitz RJ, Skiniotis G (2020) Structure of the M2 muscarinic receptor- $\beta$ -arrestin complex in a lipid nanodisc. *Nature* 579:297–302
- Wisler JW, Xiao K, Thomsen ARB, Lefkowitz RJ (2014) Recent developments in biased agonism. *Curr Opin Cell Biol* 27:18–24
- Yang F, Yu X, Liu C, Qu C-X, Gong Z, Liu H-D, Li F-H, Wang H-M, He D-F, Yi F et al (2015) Phospho-selective mechanisms of arrestin conformations and functions revealed by unnatural amino acid incorporation and 19F-NMR. *Nat Commun* 6:8202
- Yun Y, Kim DK, Seo M-D, Kim K-M, Chung KY (2015) Different conformational dynamics of  $\beta$ -arrestin1 and  $\beta$ -arrestin2 analyzed by hydrogen/deuterium exchange mass spectrometry. *Biochem Biophys Res Commun* 457:50–57
- Zhai R, Wang Z, Chai Z, Niu X, Li C, Jin C, Hu Y (2023) Distinct activation mechanisms of beta-arrestin-1 revealed by (19)F NMR spectroscopy. *Nat Commun* 14:7865
- Zhan X, Gimenez LE, Gurevich VV, Spiller BW (2011a) Protein Data Bank. Structure of bovine beta-arrestin 2. (<https://www.rcsb.org/structure/3P2D>) [DATASET]
- Zhan X, Gimenez LE, Gurevich VV, Spiller BW (2011b) Crystal structure of arrestin-3 reveals the basis of the difference in receptor binding between two non-visual subtypes. *J Mol Biol* 406:467–478
- Zhao Y, Fan Y, Daolai Z, Zhixin L, Amy L, Chuan L, Peng X, Xiao Y, Jin-Peng S (2017) Phosphorylation of G protein-coupled receptors: from the barcode hypothesis to the flute model. *Mol Pharmacol* 92:201
- Zhou XE, He Y, de Waal PW, Gao X, Kang Y, Van Eps N, Yin Y, Pal K, Goswami D, White TA et al (2017) Identification of phosphorylation codes for arrestin recruitment by G protein-coupled receptors. *Cell* 170:457–469.e413

## Acknowledgements

This work was supported by grants from the National Research Foundation of Korea, funded by the Korean government (NRF-2021R1A2C3003518 and NRF-2019R1A5A2027340 to KYC) and by a grant from the Ministry of Oceans and Fisheries' R&D project, Korea (2021633 to KYC).

## Author contributions

**Kiae Kim:** Data curation; Formal analysis; Writing—original draft. **Ka Young Chung:** Conceptualization; Data curation; Formal analysis; Supervision; Funding acquisition; Investigation; Writing—original draft; Project administration.

Source data underlying figure panels in this paper may have individual authorship assigned. Where available, figure panel/source data authorship is listed in the following database record: [biostudies:S-SCDT-10\\_1038-544319-024-00239-x](https://biostudies.org/studies/S-SCDT-10_1038-544319-024-00239-x).

## Disclosure and competing interests statement

Kiae Kim and Ka Young Chung has a patent pending for  $\beta$ arr C-tail release assay.

**Open Access** This article is licensed under a Creative Commons Attribution 4.0 International License, which permits use, sharing, adaptation, distribution and reproduction in any medium or format, as long as you give appropriate credit to the original author(s) and the source, provide a link to the Creative Commons licence, and indicate if changes were made. The images or other third party material in this article are included in the article's Creative Commons licence, unless indicated otherwise in a credit line to the material. If material is not included in the article's Creative Commons licence and your intended use is not permitted by statutory regulation or exceeds the permitted use, you will need to obtain permission directly from the copyright holder. To view a copy of this licence, visit <http://creativecommons.org/licenses/by/4.0/>. Creative Commons Public Domain Dedication waiver <http://creativecommons.org/public-domain/zero/1.0/> applies to the data associated with this article, unless otherwise stated in a credit line to the data, but does not extend to the graphical or creative elements of illustrations, charts, or figures. This waiver removes legal barriers to the re-use and mining of research data. According to standard scholarly practice, it is recommended to provide appropriate citation and attribution whenever technically possible.

© The Author(s) 2024

# Expanded View Figures

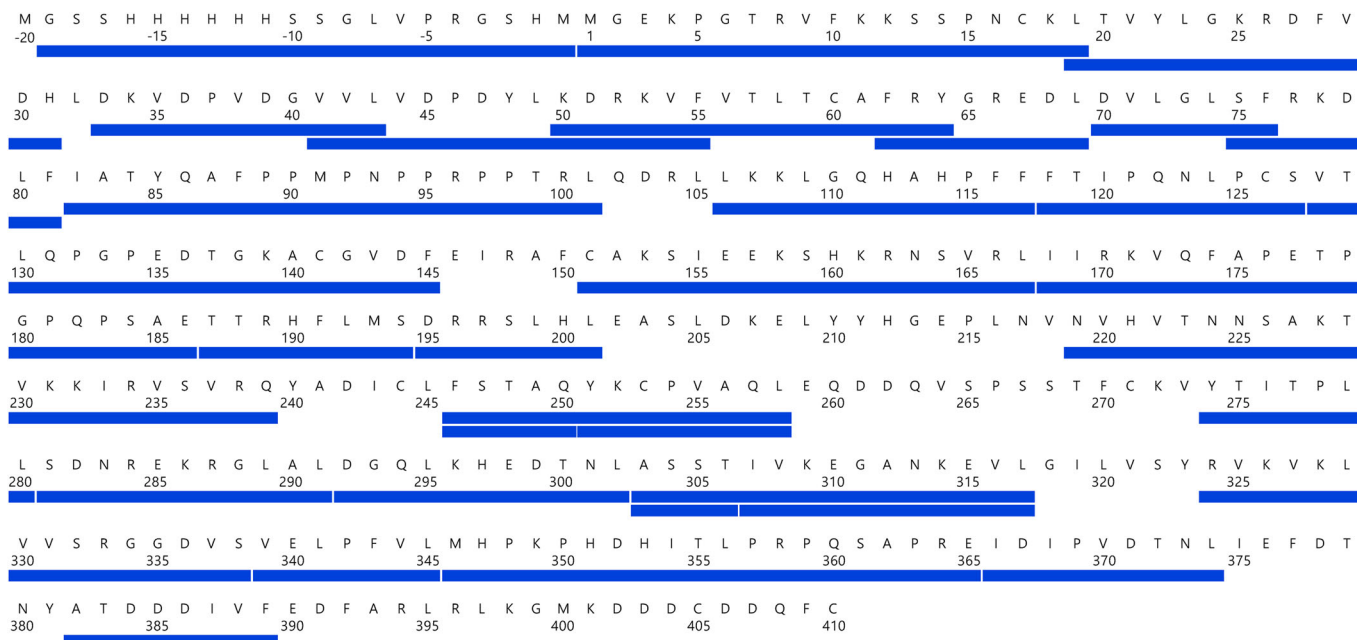


**Figure EV1. Sequence coverage map of wild-type  $\beta$ -arrestin-2 ( $\beta$ arr2).**

The blue bars indicate analyzed peptic peptides.

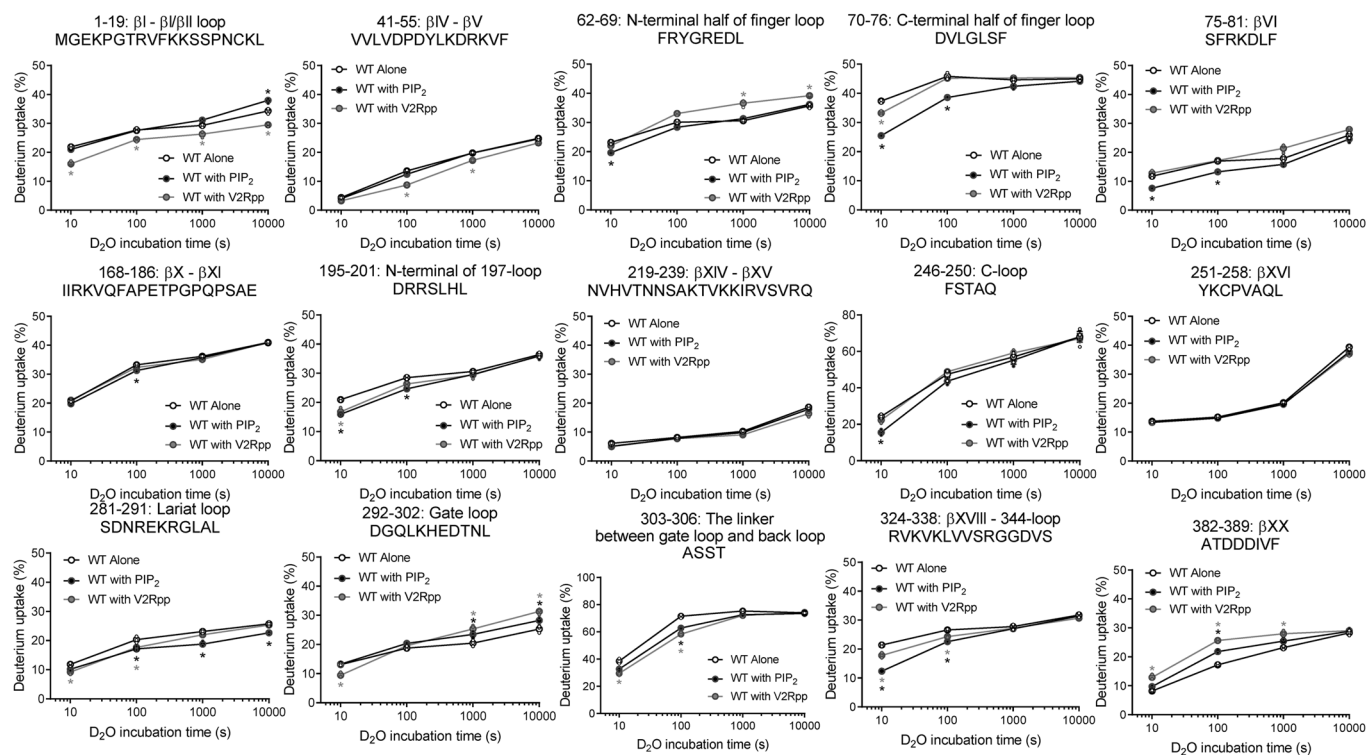


**Figure EV2. Deuterium uptake plots of selective peptides of WT  $\beta$ arr2 with or without V2Rpp or PIP<sub>2</sub> co-incubation.**

Results were derived from three independent experiments. The statistical significance of the differences was determined using Student's *t* test (\**P* < 0.05). Exact *p*-values are provided in Dataset EV1. Data are presented as mean  $\pm$  standard error of the mean. Black or grey \* indicates statistically significant difference between apo WT  $\beta$ arr2 and PIP<sub>2</sub>-bound WT  $\beta$ arr2 or V2Rpp-bound WT  $\beta$ arr2, respectively. Smaller symbols indicate each data point.

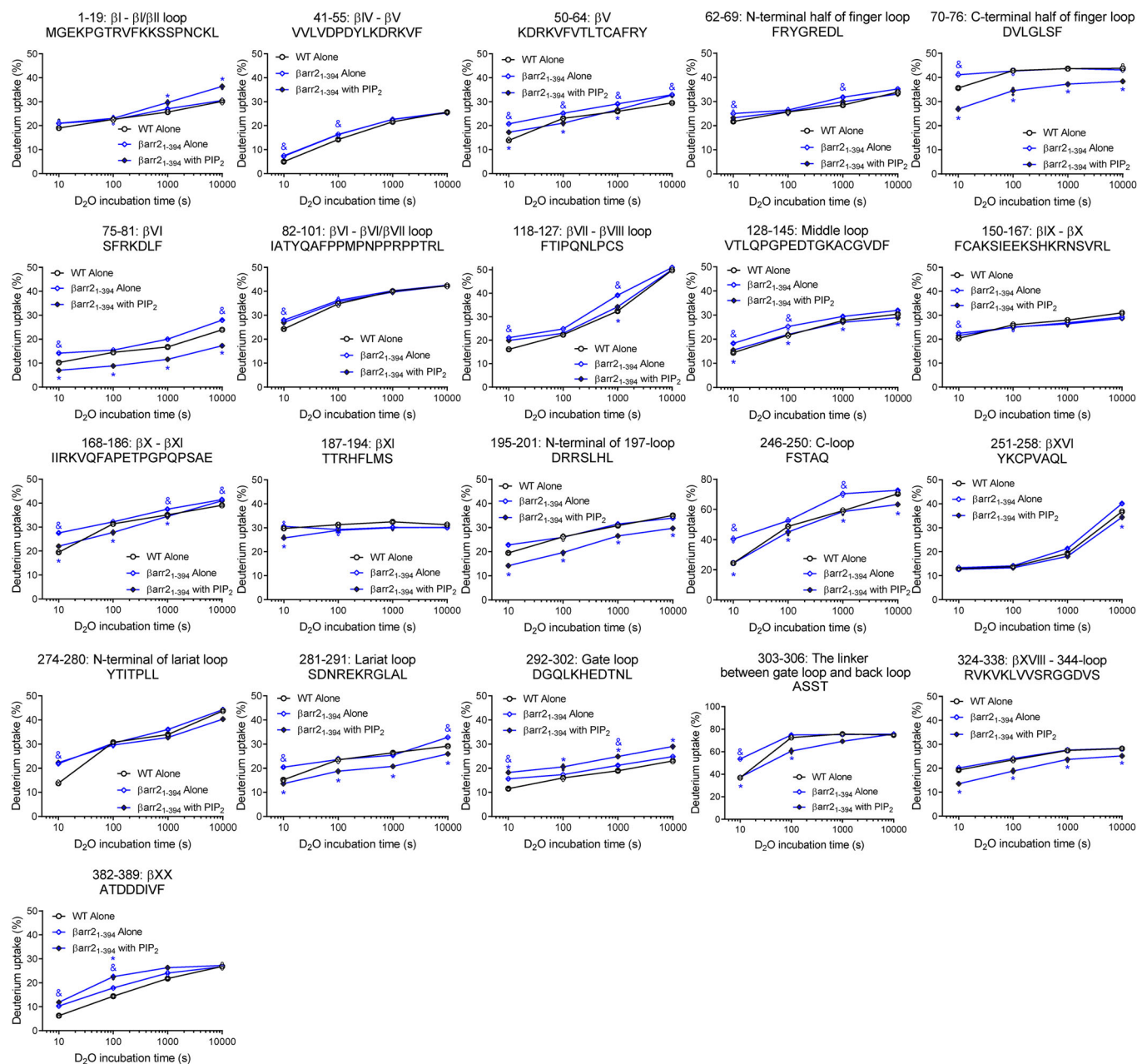


**Figure EV3. Deuterium uptake plots of selective peptides of apo WT  $\beta$ arr2 and  $\beta$ arr2<sub>1-394</sub> with or without PIP<sub>2</sub> co-incubation.**

Results were derived from three independent experiments. The statistical significance of the differences was determined using Student's *t* test (&#x26;\**P* < 0.05). Exact *p*-values are provided in Dataset EV1. &#x26; indicates statistically significant difference between apo WT  $\beta$ arr2 and apo  $\beta$ arr2<sub>1-394</sub>. \* indicates statistically significant difference between apo and PIP<sub>2</sub>-bound  $\beta$ arr2<sub>1-394</sub>. Data are presented as mean  $\pm$  standard error of the mean. Smaller symbols indicate each data point.

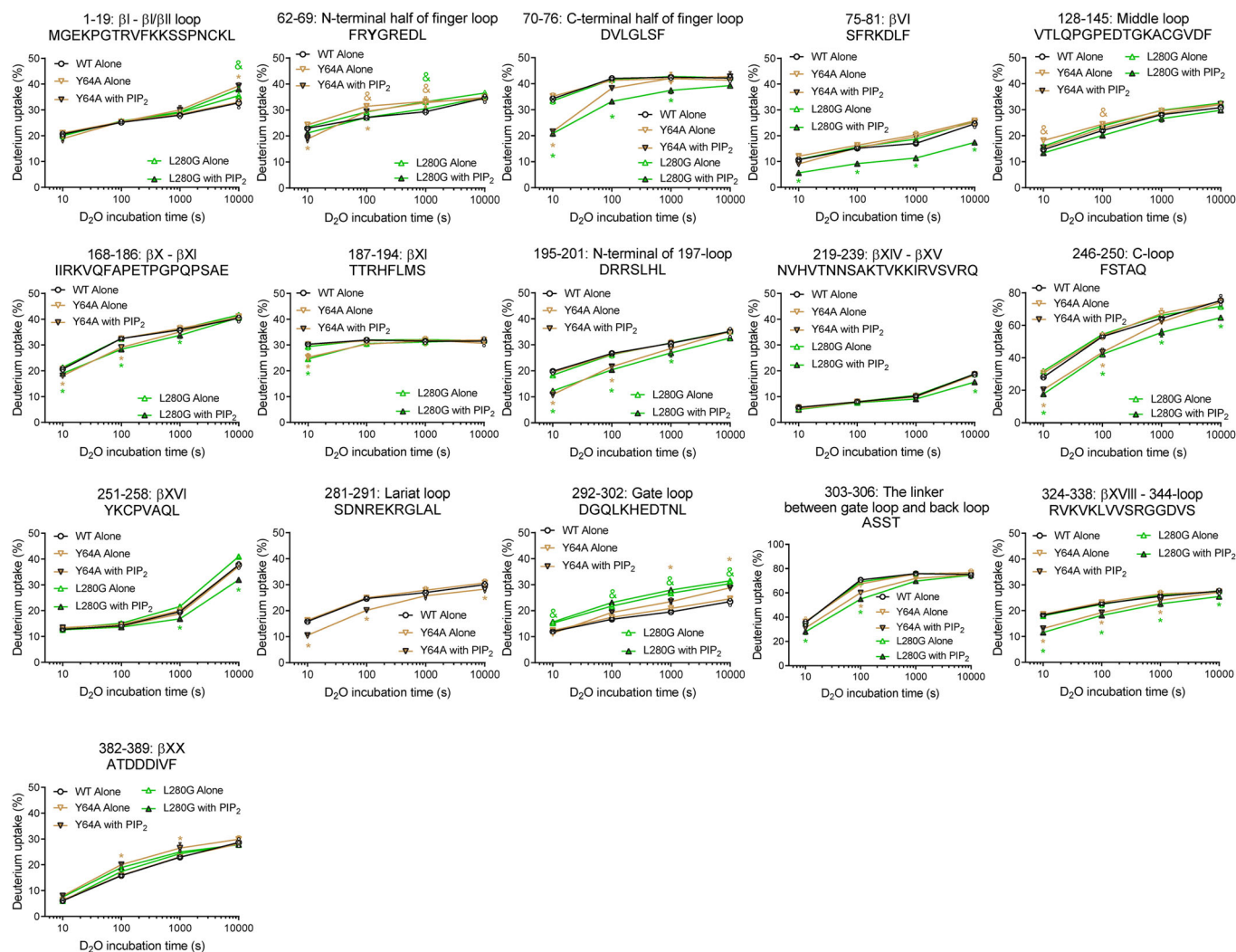


**Figure E4. Deuterium uptake plots of selective peptides of apo WT  $\beta$ arr2 and Y64A and L280G with or without PIP<sub>2</sub> co-incubation.**

Results were derived from three independent experiments. The statistical significance of the differences was determined using Student's *t* test ( $^{\&}P < 0.05$ ). Exact *p*-values are provided in Dataset EV1. Yellow green & indicates statistically significant difference between apo WT  $\beta$ arr2 and apo Y64A or L280G, respectively. Yellow or green \* indicates statistically significant difference between apo and PIP<sub>2</sub>-bound Y64A or L280G, respectively. Data are presented as mean  $\pm$  standard error of the mean. Smaller symbols indicate each data point.

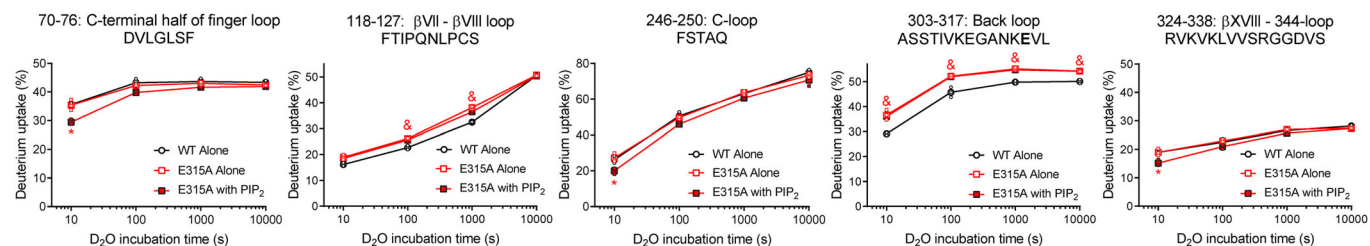


**Figure EV5. Deuterium uptake plots of selective peptides of apo WT  $\beta$ arr2 and E315A with or without PIP<sub>2</sub> co-incubation.**

Results were derived from three independent experiments. The statistical significance of the differences was determined using Student's *t* test ( $^{*}P < 0.05$ ). Exact *p*-values are provided in Dataset EV1. & indicates statistically significant difference between apo WT  $\beta$ arr2 and apo E315A. \* indicates statistically significant difference between apo and PIP<sub>2</sub>-bound E315A. Data are presented as mean  $\pm$  standard error of the mean. Smaller symbols indicate each data point.